We are IntechOpen,
the world's leading publisher of
Open Access books
Built by scientists, for scientists

4,800
Open access books available

122,000
International authors and editors

135M
Downloads

Our authors are among the

154
Countries delivered to

TOP 1%
most cited scientists

12.2%
Contributors from top 500 universities

CLARIVATE ANALYTICS
BOOK CITATION INDEX
INDEXED

WEB OF SCIENCE™

Selection of our books indexed in the Book Citation Index
in Web of Science™ Core Collection (BKCI)

Interested in publishing with us?
Contact book.department@intechopen.com

Numbers displayed above are based on latest data collected.
For more information visit www.intechopen.com

Interference Pattern Representation on the Complex s-Plane

José Trinidad Guillen Bonilla, Alex Guillen Bonilla,
Mario Alberto García Ramírez, Gustavo Adolfo Vega Gómez,
Héctor Guillen Bonilla, María Susana Ruiz Palacio,
Martín Javier Martínez Silva
and Verónica María Bettancourt Rodriguez

Abstract

In this work, the normalized interference pattern produced by a coherence interferometer system was represented as a complex function. The Laplace transform was applied for the transformation. Poles and zeros were determined from this complex function, and then, its pole-zero map and its Bode diagram were proposed. Both graphical representations were implemented numerically. From our numerical results, pole location and zero location depend on the optical path difference (OPD), while the Bode diagram gives us information about the OPD parameter. Based on the results obtained from the graphical representations, the coherence interferometer systems, the low-coherence interferometer systems, the interferometric sensing systems, and the fiber optic sensors can be analyze on the complex s-plane.

Keywords: coherence interferometer system, Laplace transform, complex function, pole-zero map, Bode diagram, graphical representations

1. Introduction

Many coherence interferometers systems find practical applications for the physical parameter measurement, such as are temperature, strain, humidity, pressure, level, current, voltage, and vibration [1–10]. Physical implementation and signal demodulation are very important for the good measurement. Many implementations are based on the Bragg gratings, fiber optics, vacuum, mirrors, crystals, polarizer, and their combinations [11–15]; whereas in the signal demodulation, has been applied commonly the Fourier transform [16–20]. This transform permits us to know all frequency components of any interference pattern, doing possible the signal demodulation for the interferometer systems.

The Laplace transform has many practical applications in topics such as control systems, electronic circuit analysis, mechanic systems, electric circuit system, pure mathematics, and communications. The linear transformation permits us to

transform any time function into a complex function whose variable is $s = i\omega + \sigma$, where i is the complex operator, ω is the angular frequency, and σ is a real value. The complex function can represent in the complex s-plane, where their axes represent the real and imaginary parts of the complex variable s. This complex plane does feasible the study of dynamic systems, and some applications are the tuning closed-loop, stability, mathematical methods, fault detection, optimization, and filter design [21–23]. In addition, the s-plane permits graphical methods such as pole-zero map, Bode diagrams, root locus, polar plots, gain margin and phase margin, Nichols charts, and N circles [24].

In dynamic system analysis, pole-zero map and Bode diagrams are two graphical methods which have many practical applications. Both methods require a complex function, where the frequency response plays a very important role. In the pole-zero map, poles and zeros have been calculated from the complex function, and then, their locations are represented on the complex s-plane. It is usual to mark a zero location by a circle (◇) and a pole location a cross (×) [24]. In the Bode diagram, the magnitude and phase are calculated from the complex function, and then, both parameters are graphed. The graphic is logarithmic, and it shows the frequency response of our system under study.

Under our knowledge, the coherence interferometer system was not studied on the s-plane, and as a consequence, its interference pattern was not represented over the pole-zero map or Bode diagrams. In this work, the complex s-plane was used to represent the output signal of an interferometer system. Applying two graphical methods, such as pole-zero plot and Bode plot, the optical signal was represented. Numerically was verified that the pole location and the zero location depend directly on the optical path difference, while a Bode diagram shows the stability/instability of the interferometer.

2. Interference pattern

Figure 1 shows a schematic example of a Michelson interferometer [25]. The interferometer consists of a coherent source, an oscilloscope, a generator function, a beam splitter 50/50 and a PZT optical element. This interferometric system has
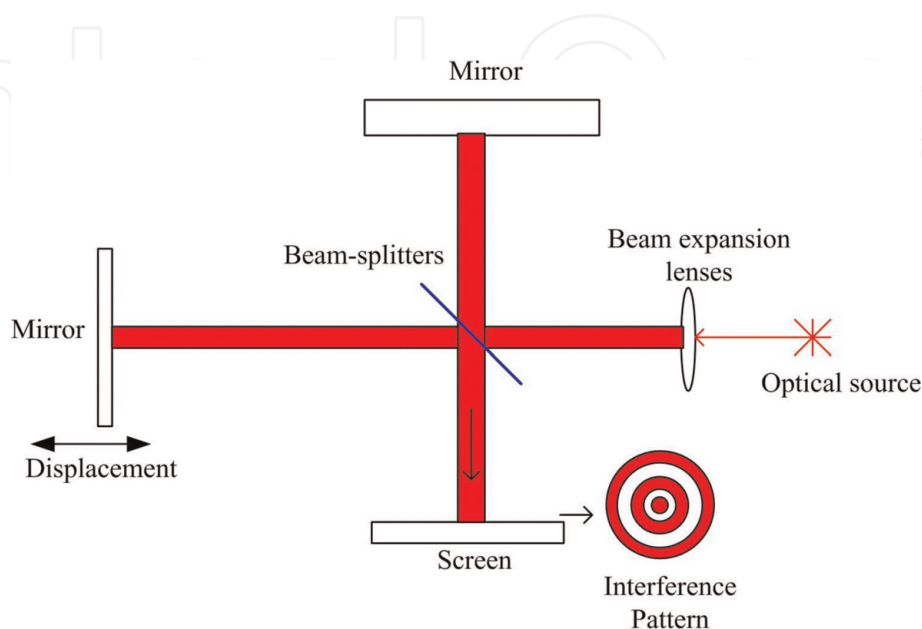

Figure 1.
Michelson interometer system.

two ways and its difference produces the optical path difference. The first one will be the reference. Its electrical field is

$$E_R(t) = A_R e^{i(\omega t + \varphi_R)}. \tag{1}$$

The second one is the signal measurement and its electrical field is

$$E_D(t) = A_D e^{i(\omega t + \varphi_D)}. \tag{2}$$

A_R and A_D are amplitudes, ω is the angular frequency, t is the time, and φ_R and φ_D are given by

$$\varphi_R = 2k x_R, \tag{3}$$

and

$$\varphi_D = 2k x_D. \tag{4}$$

x_R and x_D are the distances traveled by both beams and $k = \frac{2\pi n}{\lambda}$ is the wavenumber: λ is the wavelength and n is the refraction index.

From **Figure 1**, when the photodetector detects the total field, its signal is

$$E_T(t) = A_R e^{i(\omega t + \varphi_R)} + A_D e^{i(\omega t + \varphi_D)}. \tag{5}$$

Following, the irradiance E_T^2 will be

$$E_T^2 = \left[A_R e^{i(\omega t + \varphi_R)} + A_D e^{i(\omega t + \varphi_D)} \right] \left[A_R e^{-i(\omega t + \varphi_R)} + A_D e^{-i(\omega t + \varphi_D)} \right]. \tag{6}$$

Developing, we will obtain

$$E_T^2 = E_R^2 + E_D^2 + E_R E_D \left[e^{i(\omega t + \varphi_R)} e^{-i(\omega t + \varphi_D)} + e^{i(\omega t + \varphi_D)} e^{-i(\omega t + \varphi_R)} \right] \tag{7}$$

or

$$E_T^2 = E_R^2 + E_D^2 + E_R E_D \left[e^{i(\varphi_R - \varphi_D)} + e^{-i(\varphi_R - \varphi_D)} \right]. \tag{8}$$

Using the identity $cos(\theta) = \frac{e^{i\theta} + e^{-i\theta}}{2}$, Eq. (8) takes the form

$$E_T^2 = E_R^2 + E_D^2 + 2 E_R E_D \cos(\varphi_R - \varphi_D). \tag{9}$$

In terms of intensity, the interferometer system produces the next interference pattern

$$I_T = I_R + I_D + 2\sqrt{I_R I_D} \cos(\varphi_R - \varphi_D). \tag{10}$$

If both beams have the same intensity $I_R = I_D = I_o$, the total intensity will take the form

$$I_T = 2I_o[1 + \cos(\varphi_R - \varphi_D)]. \tag{11}$$

As seen in Eq. (11), the phase difference is due to the optical path difference between the two beams. Substituting Eqs. (3) and (4) into Eq. (11), the interference pattern in terms of intensity can be written as

$$I_T(t) = 2I_o \left[1 + \cos \left(\frac{4\pi n}{\lambda} \Delta x(t) \right) \right], \qquad (12)$$

where $\Delta x = x_R - x_D$ is the length difference between the distances x_R and x_D. Basically, the irradiance is an interference pattern which is formed by two functions: enveloped and modulate. The enveloped function is $f_{env} = 2I_o \left[\frac{W}{m^2} \right]$ and this function contains information from the optical source. The modulate function is given by $f_{mod} = 1 + \cos \left(\frac{4\pi n}{\lambda} \Delta x(t) \right)$ and it contains information about the interference pattern. The modulate function consist of a constant (direct component) and a trigonometric function (cosine function) whose frequency depends on the optical path difference.

3. Complex function

Observing **Figure 1** and Eq. (11), the phase difference $\varphi_R - \varphi_D$ is a time-varying function, and as a consequence, the phase $\frac{4\pi n}{\lambda} \Delta x(t)$ is also a time-varying function. In this case, the instantaneous output voltage (or current) of our photodector is proportional to the normalized optical intensity $\frac{I_T(t)}{I_o}$, where I_o is the LASER intensity $\left[\frac{W}{m^2} \right]$ [25]. Mathematically, the normalized interference pattern can be written as

$$I_n(t) = \frac{I_T(t)}{I_o} = 2[1 + \cos(\omega_m t)]. \qquad (13)$$

Here, the angular frequency ω_m was proposed from the phase $\frac{4\pi n}{\lambda} \Delta x(t)$ and the interferometer system has not external perturbations.

To determinate the complex function $I_n(s)$, we calculate the unilateral Laplace transform for our last expression

$$I_n(s) = \int_0^\infty I_n(t) e^{-st} dt = 2 \int_0^\infty e^{-st} dt + 2 \int_0^\infty \cos(\omega_m t) e^{-st} dt. \qquad (14)$$

Substituting the trigonometric identity $\cos(\omega_m t) = \frac{e^{i\omega_m t} + e^{-i\omega_m t}}{2}$ into Eq. (14), the complex function can be estimated through

$$I_n(s) = 2 \int_0^\infty e^{-st} dt + 2 \int_0^\infty \left(\frac{e^{i\omega_m t} + e^{-i\omega_m t}}{2} \right) e^{-st} dt, \qquad (15)$$

or

$$I_n(s) = 2 \int_0^\infty e^{-st} dt + \int_0^\infty e^{i\omega_m t} e^{-st} dt + \int_0^\infty e^{-i\omega_m t} e^{-st} dt. \qquad (16)$$

Solving the integrals, the complex function will be

$$I_n(s) = -\frac{2}{s} e^{-st} \Big|_0^\infty + \frac{e^{-(-i\omega_m t + s)t}}{-(-i\omega_m t + s)} \Big|_0^\infty + \frac{e^{-(i\omega_m + s)t}}{-(i\omega_m + s)} \Big|_0^\infty. \qquad (17)$$

Evaluating the limits,

$$I_n(s) = \frac{2}{s} + \frac{1}{s - i\omega_m} + \frac{1}{s + i\omega_m}. \tag{18}$$

Using the algebraic procedure, we obtain

$$I_n(s) = \frac{2}{s} + \frac{s + i\omega_m + s - i\omega_m}{s^2 - i^2\omega_m^2} = \frac{2}{s} + \frac{2s}{s^2 + \omega_m^2}. \tag{19}$$

As seen in Eq. (19), the first term was produced by the direct component and the second term was produced by cosine function. Now, let us represent the complex function as

$$I_n(s) = \frac{4s^2 + 2\omega_m^2}{s(s^2 + \omega_m^2)}. \tag{20}$$

Because the Laplace transform was used for the transformation, the normalized interference pattern can be studied in the time domain and on a complex s-plane. It is possible since both Eqs. (13) and (20) contain the same information.

4. Graphical representation

In mathematics and engineering, the s-plane is the complex plane which Laplace transform is graphed. It is a mathematical domain where, instead of view processes in the time domain modeled with time-based functions, they are viewed as equations in the frequency domain. Then, the function $I_n(s)$ can be graphed using the pole-zero map and the Bode diagrams. These graphical representations provide a basis for determining important system response characteristics.

4.1 Pole-zero plot

In general, the poles and zeros of a complex function may be complex, and the system dynamics may be represented graphically by plotting their locations on the complex s-plane, whose axes represent the real and imaginary parts of the complex variable s. Such graphics are known as pole-zero plots. It is usual to mark a zero location by a circle ($\diamond$) and a pole location a cross ($\times$). In this study, it is convenient to factor the polynomials in the numerator and denominator and to write the complex function in terms of those factors

$$I_n(s) = \frac{P_N(s)}{P_D(s)} = \frac{4s^2 + 2\omega_m^2}{s(s^2 + \omega_m^2)}, \tag{21}$$

where the numerator and denominator polynomials, $P_N(s)$ and $P_D(s)$, have real coefficient defined by the system's characteristic. To calculate the zeros, we require

$$P_N(s) = 0 = 4s^2 + 2\omega_m^2. \tag{22}$$

Solving last polynomial function, the roots (zeros) are localized at

$$s^2 = \frac{-\omega_m^2}{2} \rightarrow s = \sqrt{-\frac{\omega_m^2}{2}}. \tag{23}$$

From our last results, the zeros are imaginary values

$$
\begin{aligned}
s_1 &= i\frac{\omega_m}{\sqrt{2}} \\
s_2 &= -i\frac{\omega_m}{\sqrt{2}}
\end{aligned}.
\tag{24}
$$

By the similar way,

$$
P_D(s) = 0 = s\left(s^2 + \omega_m^2\right).
\tag{25}
$$

To calculate the roots,

$$
\begin{aligned}
s_1 &= 0 \\
s_2 &= i\omega_m \\
s_3 &= -i\omega_m
\end{aligned}.
\tag{26}
$$

Using our previous results presented at Eq. (24) and Eq. (26), we represent a pole-zero plot for the interference pattern, see **Figure 2**.

From **Figure 2**, the interference pattern produces two zeros and three poles. Both zeros (s_1 *and* s_2) and two poles (s_2 *and* s_3) are over the imaginary axes and their locations depend on the angular frequency. The pole (s_1) was obtained by the direct component; our normalized interference pattern and the location are over the origin.

4.2 Bode diagram

Based on the system theory and system graphic representation, the complex interference pattern can be represented through the Bode diagram. The graphical representation permits us to graph the frequency response of our interferometer system. It combines a Bode magnitude plot, expressing the magnitude (decibels) of the frequency response, and a Bode phase plot, expressing the phase shift.
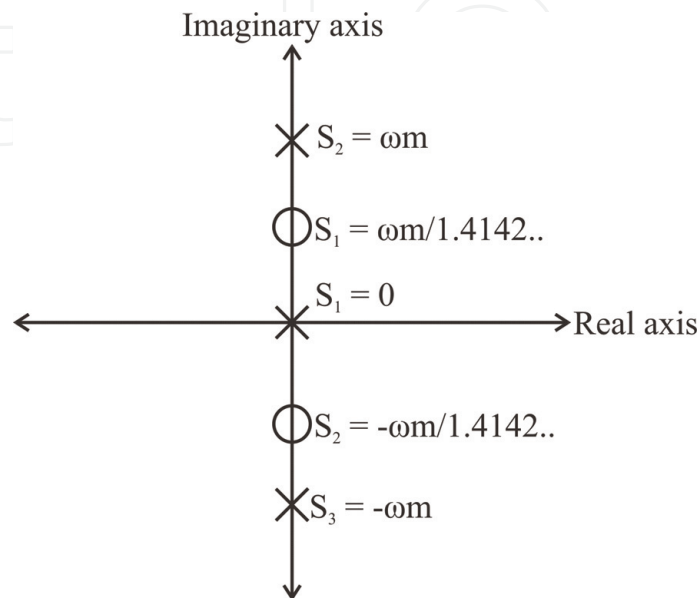

Figure 2.
Polo-zero map obtained from the interference pattern.

As was mentioned, the complex interference pattern can be represented through the Bode diagram. To represent it, the term s is substituted by the term $i\omega$: i is the complex number and ω is the angular frequency. Such that, Eq. (20) takes the form

$$I_n(i\omega) = I_n(\omega) = \frac{2\left[2(i\omega)^2 + \omega_m^2\right]}{i\omega\left[(i\omega)^2 + \omega_m^2\right]}. \tag{27}$$

The magnitude (in decibels) of the transference function above is given by decibels gain expression:

$$A_{vdB} = 20 \, log \, |I_n(i\omega)|. \tag{28}$$

Substituting Eq. (27) into Eq. (28), the magnitude will be

$$A_{vdB} = 20 \, log \, \left|\frac{2\left[2(i\omega)^2 + \omega_m^2\right]}{i\omega\left[(i\omega)^2 + \omega_m^2\right]}\right|. \tag{29}$$

Applying the logarithm rules, Eq. (29) can express as

$$A_{vdB} = 20 \, log \, (2) + 20 \, log \, \left(\left|2(i\omega)^2 + \omega_m^2\right|\right) - 20 \, log \, (|i\omega|)$$
$$-20 \, log \, \left(\left|(i\omega)^2 + \omega_m^2\right|\right). \tag{30}$$

To determine the phase, Eq. (27) will express as

$$I_n(i\omega) = \frac{-4\omega^2 + 2\omega_m^2}{i\left[-\omega^3 + \omega\omega_m^2\right]}. \tag{31}$$

Here, $i^2 = -1$ was used. Last expression can be written as

$$I_n(i\omega) = -i\frac{-4\omega^2 + 2\omega_m^2}{\left[-\omega^3 + \omega\omega_m^2\right]}. \tag{32}$$

From Eq. (32), the phase can also be determined.

5. $I_n(t)$ retrieval

As the Laplace transform is a linear transformation, during the transformation: $I_n(t) \rightarrow I_n(s)$ and $I_n(s) \rightarrow I_n(t)$, the information is not lost and then the interference pattern can be studied in the time domain and on the complex s-plane. In Section 2, it was explained the transformation $I_n(t) \rightarrow I_n(s)$, and their poles and zeros were graphed over the pole-zero map. In addition, we developed interference pattern on the frequency plane, being possible to implement the Bode plot. Following, we recover the time function from the complex function $I_n(s) \rightarrow I_n(t)$. This section is didactic since the objective is to verify that the complex function's information can also be represented in the time domain.

To recover the time function, we calculate the inverse Laplace transform through

$$I_n(t) = \frac{1}{2\pi i} \lim_{T\to\infty} \int_{\gamma-iT}^{\gamma+iT} I_n(s)e^{st}ds = \mathcal{L}^{-1}\{I_n(s)\}. \tag{33}$$

The integral complex is in the s-plane; their limits are $\gamma - iT$ and $\gamma + iT$; the symbol $\mathcal{L}^{-1}\{\cdot\} = \frac{1}{2\pi i} \lim_{T\to\infty} \int_{\gamma-iT}^{\gamma+iT} \{\cdot\}e^{st}ds$ indicates the inverse Laplace transform. Substituting Eq. (21) into Eq. (33), the normalized interference pattern can be obtained by

$$I_n(t) = \frac{1}{2\pi i} \lim_{T\to\infty} \int_{\gamma-iT}^{\gamma+iT} \frac{4s^2 + 2\omega_m^2}{s\left(s^2 + \omega_m^2\right)}e^{st}ds = \mathcal{L}^{-1}\left\{\frac{4s^2 + 2\omega_m^2}{s\left(s^2 + \omega_m^2\right)}\right\}. \tag{34}$$

Applying the partial fraction, Eq. (34) can be expressed as

$$I_n(t) = \frac{1}{2\pi i} \lim_{T\to\infty} \int_{\gamma-iT}^{\gamma+iT} \left(\frac{A}{s} + \frac{Bs + C}{s^2 + \omega_m^2}\right)e^{st}ds = \mathcal{L}^{-1}\left\{\frac{A}{s} + \frac{Bs + C}{s^2 + \omega_m^2}\right\}. \tag{35}$$

Here, A, B, and C are constants. To calculate the constant, we use next equality

$$\frac{4s^2 + 2\omega_m^2}{s\left(s^2 + \omega_m^2\right)} = \frac{A}{s} + \frac{Bs + C}{s^2 + \omega_m^2} \rightarrow 4s^2 + 2\omega_m^2 = As^2 + A\omega_m^2 + Bs^2 + Cs \tag{36}$$

Using Eq. (36), we obtain the next equation system and their solutions as

$$\begin{aligned} (A + B)s^2 &= 4s^2 & A &= 2 \\ Cs &= 0 & \rightarrow \quad B &= 2 \, . \\ A\omega_m^2 &= 2\omega_m^2 & C &= 0 \end{aligned} \tag{37}$$

Substituting all constants into Eq. (37), the time function will be

$$I_n(t) = \mathcal{L}^{-1}\left\{\frac{2}{s}\right\} + \mathcal{L}^{-1}\left\{\frac{2s}{s^2 + \omega_m^2}\right\}. \tag{38}$$

Laplace transform		Inverse Laplace transform	
Time function	Complex function	Complex function	Time function
$f(t) = ku(t)$	$F(s) = \frac{k}{s}$	$F(s) = \frac{k}{s}$	$f(t) = ku(t)$
$f(t) = tu(t)$	$F(s) = \frac{1}{s^2}$	$F(s) = \frac{k}{s}$	$f(t) = tu(t)$
$f(t) = t^n u(t)$	$F(s) = \frac{n!}{s^{n+1}}$	$F(s) = \frac{n!}{s^{n+1}}$	$f(t) = t^n u(t)$
$f(t) = \cos(\omega t)u(t)$	$F(s) = \frac{s}{s^2 + \omega^2}$	$F(s) = \frac{s}{s^2 + \omega^2}$	$f(t) = \cos(\omega)u(t)$
$f(t) = sen(\omega t)u(t)$	$F(s) = \frac{\omega}{s^2 + \omega^2}$	$F(s) = \frac{\omega}{s^2 + \omega^2}$	$f(t) = sen(\omega t)u(t)$
$f(t) = \cosh(\omega t)u(t)$	$F(s) = \frac{s}{s^2 - \omega^2}$	$F(s) = \frac{s}{s^2 - \omega^2}$	$f(t) = \cosh(\omega)u(t)$
$f(t) = senh(\omega t)u(t)$	$F(s) = \frac{\omega}{s^2 - \omega^2}$	$F(s) = \frac{\omega}{s^2 - \omega^2}$	$f(t) = senh(\omega t)u(t)$

Note: $u(t)$ is the Heaviside function.

Table 1.
Fundamental Laplace transform [24].

Applying **Table 1**, the solved inverse Laplace transform is

$$I_n(t) = 2[1 + \cos(\omega_m t)]. \tag{39}$$

Observing both Eq. (13) and Eq. (39), we recover the time function from the complex function. Thus, we confirm that the complex s-plane permits us to study the interferometer system through the complex s-plane, using the pole-zero map and Bode diagrams.

6. Numerical results and discussion

6.1 Results

To verify our proposal, we consider the next interference pattern

$$I_T(t) = 2e^{t^2}[1 + \cos(10t)]. \tag{40}$$

From Eq. (40), the enveloped f_{env} is a Gaussian function $\left(f_{env} = 2I_o = 2e^{t^2}\right)$ and the modulate function is $f_{mod} = 1 + \cos(10t)$, where the angular frequency is $\omega_m = 10 \left[\frac{radians}{se}\right]$. If the interference pattern is normalized as Eq. (12), we obtain

$$I_n(t) = \frac{I_T(t)}{I_o} = 2[1 + \cos(10t)]. \tag{41}$$

Figure 3 shows the interference pattern and the modulate function. Calculating the Laplace transform,

$$I_n(s) = \frac{P_N(s)}{P_D(s)} = \frac{4s^2 + 200}{s(s^2 + 100)}. \tag{42}$$

Using Expressions (24) and (42), the zeros are localized at the points

$$\begin{aligned} s_1 &= i\frac{10}{\sqrt{2}} \\ s_2 &= -i\frac{10}{\sqrt{2}} \end{aligned}. \tag{43}$$

Now, using Eqs. (26) and (42), the poles are

$$\begin{aligned} s_1 &= 0 \\ s_2 &= i10 \\ s_3 &= -i10. \end{aligned} \tag{44}$$

Finally, its pole-zero map can observe in **Figure 4**.

As seen in **Figure 4**, the zeros (s_1 *and* s_2) and the poles (s_2 *and* s_3) are over the imaginary axis. Their positions depend on the angular frequency, and therefore, their positions change due to the variations of the optical path difference. The pole s_1 is over the origin (of the complex s-plane), and it was generated by the direct component of our interference pattern.
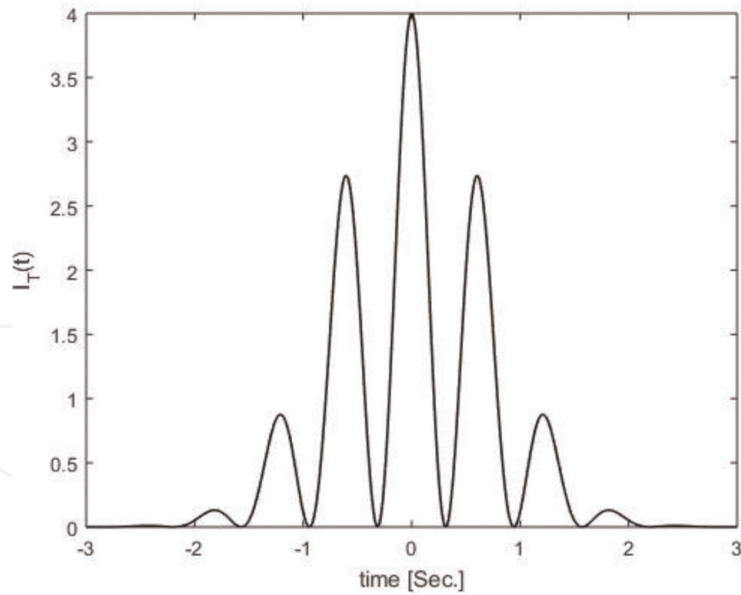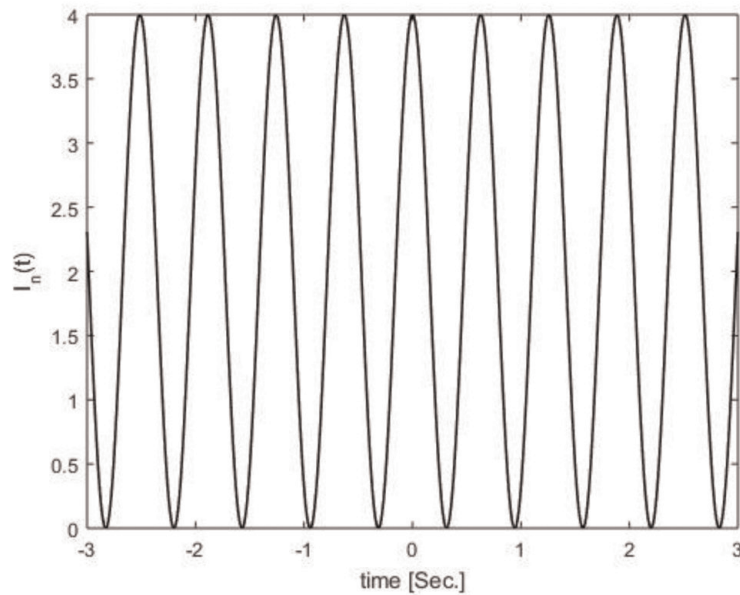
Figure 3.
(a) The simulated interference pattern. (b) The modulate function.

To generate the Bode diagram, we consider the next complex function

$$I_n(s) = \frac{4(i\omega)^2 + 200}{i\omega\left[(i\omega)^2 + 100\right]}. \tag{45}$$

Combining Eqs. (28) and (45), the magnitude (in decibels) is

$$A_{vdB} = 20\ log\left|\frac{4(i\omega)^2 + 200}{i\omega\left[(i\omega)^2 + 100\right]}\right|, \tag{46}$$

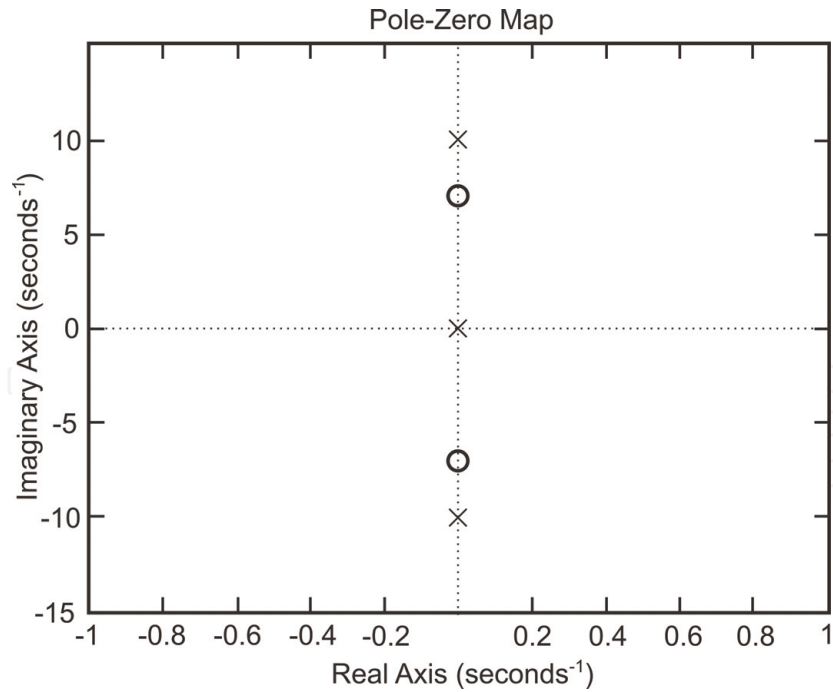where $s = i\omega$ was used. Applying the logarithm rules, the magnitude can calculate as

Figure 4.
Pole-zero plot determined from the complex modulate function (42).

$$A_{vdB} = 20 \ log \ \left(\left|4(i\omega)^2 + 200\right|\right) - 20 \ log \ (|i\omega|) - 20 \ log \ \left(\left|(i\omega)^2 + 100\right|\right). \quad (47)$$

Using the Scientific MatLab software, we represent its Bode plot, see **Figure 5**.

Observing **Figure 5**, the magnitude has a small variation between the intervals of 10^0 to $10^{0.7}$ and from 10^1 to 10^2 while the phase is -90^0. These results confirm the integrative action indicated by Eq. (47). The interferometric system produces two asymptotics for the magnitude. First asymptotic is negative, its location is at the point $10^{0.7}$ and the phase has transition from $-90°$ to 90^0. Second asymptotic
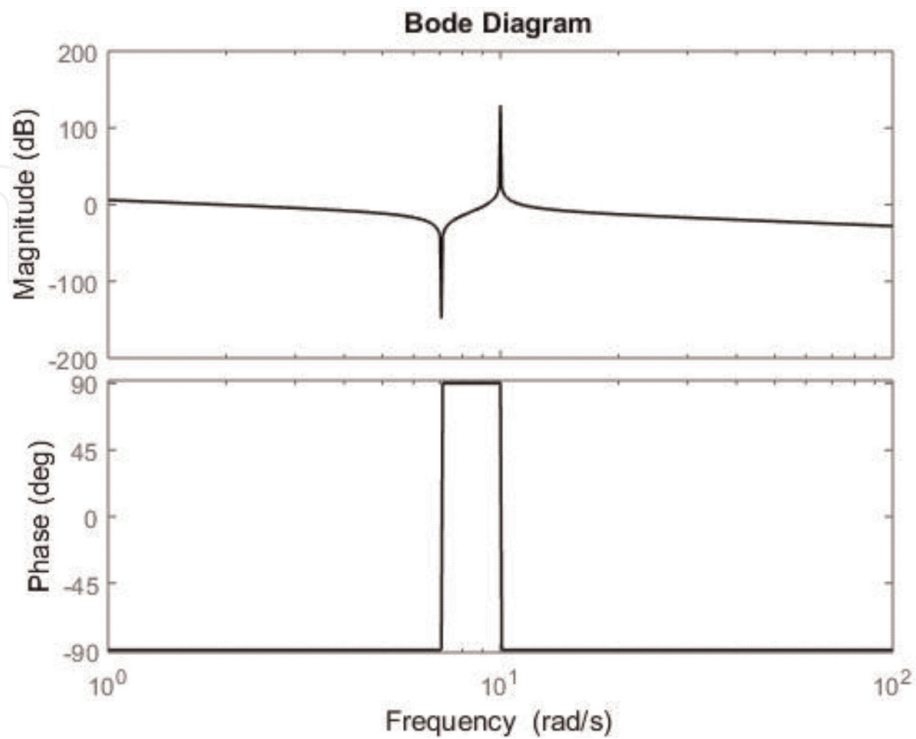

Figure 5.
Bode diagram obtained from the interference pattern.

is positive, its location is 10^1 and the phase has transition from 90^0 to -90°. Last interval is between $10^{0.7}$ and 10^1. In this case, the magnitude has small variation again but the phase is constant to 90°. These results confirm that the interferometer system will have integrative action and derivative action.

6.2 Discussion

Here, a complex function was obtained from the interference pattern produced by a coherence interferometer. Considering the pole-zero map, poles and zeros depend directly on the optical path difference of an interferometer. The interference pattern generates three poles and two zeros. A pole is over the origin and two poles are over the points $\pm i\omega_m$. The zeros are over the points $\pm i\frac{\omega_m}{\sqrt{2}}$. Now, considering the Bode plot, the interferometer can act as an integrator and as a derivator since the phase can take the value of -90° or 90°, see **Figure 5**. Both graphical representations permit to know the optical path difference through the angular frequency and its dynamic response.

From our analysis and results, it is possible to infer a few key point of our novel method.

- The complex s-plane permits us to study the interferometric systems.

- The interference pattern can represent as a complex function whose poles are three and zeros are two.

- Pole-zero map gives information about the optical path difference.

- The pole s_1 is over the origin and it was generated by the direct component of the interference pattern.

- s_2 and s_3 poles are over the imaginary axis and their position are $\pm i\omega_m$, where ω_m is the angular frequency.

- s_1 and s_2 zeros are over the imaginary axes and their locations depend on the angular frequency, see **Figure 4**.

- Bode diagram gives us information about the dynamic response of any interference pattern.

- Based on the Bode diagram (Phase information), the interferometer can act as an integrative action and as a derivative action.

Based on our results, the interference pattern can be studied by both graphical methods. Those graphical representations can be applied to low-coherence interferometric systems, optical fiber sensors, communication systems, and optical source characterization.

7. Conclusion

In this work, applying the Laplace transform and inverse Laplace transform, we confirm that the interference pattern produced by an Interferometer, can study in the time domain and on the complex s-plane. The pole-zero plot and the Bode diagram were obtained from the complex interference pattern. Both graphical

representations give us information about the interferometer. The optical Path Difference (OPD) information can measure through the pole-zero map and the behavior of interferometer can understand through the Bode diagram. Therefore, the interferometers can be studied on the complex s-plane, being possible measures physical parameters when those interferometers were disturbed. Also, the signal demodulation can be implemented for the quasi-distributed fiber sensor when the local sensors are interferometers. Some measurable parameters are temperature, string, displacement, voltage and pressure.

If a low-coherence interferometer is studied on the s-plane, then the fringe visibility and the magnitude of coherence grade can be measured.

Acknowledgements

Conflict of interest

The authors declare no conflict of interest.

Author details

José Trinidad Guillen Bonilla[1,2]*, Alex Guillen Bonilla[3],
Mario Alberto García Ramírez[1], Gustavo Adolfo Vega Gómez[1],
Héctor Guillen Bonilla[4], María Susana Ruiz Palacio[1], Martín Javier Martínez Silva[1]
and Verónica María Bettancourt Rodriguez[5]

1 Electronic Department, CUCEI, University of Guadalajara, Guadalajara, Jaliscos, Mexico

2 Mathematic Department, CUCEI, University of Guadalajara, Guadalajara, Jaliscos, Mexico

3 Department of Computer Science and Engineering, CUVAlles, University of Guadalajara, Ameca, Jalisco, Mexico

4 Department of Engineering Projects, CUCEI, University of Guadalajara, Guadalajara, Jaliscos, Mexico

5 Chemical Department, CUCEI, University of Guadalajara, Guadalajara, Jaliscos, Mexico

*Address all correspondence to: trinidad.guillen@academicos.udg.mx

IntechOpen

References

[1] Zhao N, Lin Q, Jiang Z, Yao K, Tian B, Fang X, et al. High temperature high sensitivity multipoint sensing system based on three cascade Mach-Zehnder interferometers. Sensors. 2018; **18**(8):2688. DOI: 10.3390/s18082688

[2] Jia X, Liu Z, Deng Z, Deng W, Wzng Z, Zhen Z. Dynamic absolute distance measurement by frequency sweeping interferometry based Doppler beat frequency tracking model. Optics Communication. 2019;**430**:163-169

[3] Peng J, Lyu D, Huang Q, Qu Y, Wang W, Sun T, et al. Dielectric film based optical fiber sensor using Fabry-Perot resonator structure. Optics Communication. 2019;**430**:63-69

[4] Vigneswaran D, Ayyanar VN, Sharma M, Sumahí M, Mani Rajan MS, Porsezian K. Salinity sensor using photonic crystal fiber. Sensors and Actuors A: Physical. 2018;**269**(1):22-28. DOI: 10.1016/j.sna2017.10.052

[5] Kamenev O, Kulchin YN, Petrov YS, Khiznyak RV, Romashko RV. Fiber-optic seismometer on the basis of Mach-Zehnder interfometer. Sensors and Actuors A: Physical. 2016;**244**:133-137. DOI: 10.1016/j.sna.2016.04.006

[6] Li L, Xia L, Xie Z, Liu D. All-fiber Mach-Zehnder interferometers for sensing applications. Optic Express. 2012;**20**(10):11109-11120. DOI: 10.1364/OE.20.011109

[7] Yu Q, Zhou X. Pressure sensor based on the fiber-optic extrinsic Fabry-Perot interferometer. Photonic Sensors. 2011; **1**(1):72-83. DOI: 10.1007/s13320-010-0017-9

[8] Yeo TL, Sun T, Grattan KTV. Fibre-optic sensor technologies for humidity and moisture measurement. Sensors and Actuators: Physical. 2008;**144**(2): 280-295. DOI: 10.1016/j.sna.2008.01.017

[9] Dong C, Li K, Jiang Y, Arola D, Zhang D. Evaluation of thermal expansion coefficient carbon fiber reinforced composites using electronic speckle interferometry. Optics Express. 2018;**26**(1):531. DOI: 10.1364/OE.26.000531

[10] Wang S, Gao Z, Li G, Feng Z, Feng Q. Continual mechanical vibration trajectory tracking based on electro-optical heterodyne interferometric. Optics Express. 2014;**22**(7):7799. DOI: 10.1364/OE.22.007799

[11] Wan X, Ge J, Chen Z. Development of stable monolithic wide-field Michelson interferometers. Applied Optics. 2011;**50**(21):4105-4114. DOI: 10-1364/AO.50.004105

[12] Hassan MA, Martin H, Jiang X. Development of a spatially dispersed short-coherence interferometry sensor using diffraction grating orders: Publisher's note. Applied Optics. 2018; **57**(1):5. DOI: 10.1364/AO.57.000005

[13] Guillen Bonilla JT, Guillen Bonilla A, Rodríguez Betancourtt VM, Guillen Bonilla H, Casillas Zamora A. A theoretical study and numerical simulation of a quasi-distributed sensor based on the low-finesse Fabry-Perot interferometer: Frequency-division multiplexing. Sensors. 2017;**17**(4):859. DOI: 10.3390/s17040859

[14] Liang Y, Zhao M, Wu Z, Morthier G. Investigation of grating-assisted trimodal interferometer biosensors based on a polymer platform. Sensors. 2018;**18**(5):1502. DOI: 10.3390/s.18052502

[15] Guillen Bonilla JT, Guillen Bonilla H, Casillas Zamora A, Vega Gómez GA, Franco Rodríguez NE, Guillen Bonilla A, et al. Twin-grating fiber optic sensors applied on wavelength-division multiplexing and its numerical

simulation. In: Rao SP, editor. Book of Numerical Simulation in Engineering and Science. 1st ed. IntechOpen. DOI: 10.5772/intechopen.75586

[16] de SAuza JC, Oliveira ME, Dos Santos PAM. Brach-cut algorithm for optical phase unwrapping. Optics Letters. 2015;**40**(15):3456-3459. DOI: 10.1364OL.40.003456

[17] Mizuno T, Kitoh T, Oguma M, Inoue Y, Shibata T, Hiroshi T. Mach-Zehnder interferometer with uniform wavelength period. Optics Letters. 2004;**29**(5):454-456. DOI: 10.1364/OL.29.000454

[18] Miridonov SV, Shlyagin M, Tentori D. Twin-grating fiber optic sensor demodulation. Optics Communication. 2001;**191**(3–6):253-362. DOI: 10.1016/S0030-4018(01)01160-9

[19] Kin JA, Kim JW, Kang CS, Jin J, Eom TB. Interferometric profile scanning system for measuring large planar mirror surface based on single-interferogram analysis using Fourier transform. Measurements. 2018;**118**:113-119. DOI: 10.1016/j.measurement.2018.01.023

[20] Perea J, Libbey B, Nehmetallah G. Multiaxis heterodyne vibrometer for simultaneous observation of 5 degrees of dynamic freedom from a single beam. Optics Letters. 2018;**43**(13):3120-2123. DOI: 10.1364/OL.43.003120

[21] Davoodi M, Mezkin N, Khorasani K. A single dynamic observer-based module for design of simultaneous fault detection, isolation and tracking control scheme. International Journal of Control. 2018;**91**(3):508-523. DOI: 10.1080/00207179.2017.1286041

[22] Ordóñez Hurtado RH, Crisostomi E, Shorten RN. An assessment on the use of stationary vehicles to support cooperative positioning systems. International Journal of Control. 2018; **91**(3):608-621. DOI: 10.1080/00207179.2017.1286537

[23] Xu S, Sun G, Li Z. Finite frequency vibration suppression for space flexible structures in tip position control. International Journal of Control, Automation and Systems. 2018;**16**(3):1021-1029. DOI: 10.1007/s12555-0160343-9

[24] Wolovich WA. Automatic Control Systems: Basic Analysis and Design. 1st ed. Sounders College Pub.; 1994. 450 p. ISBN: 0030237734, 9780030237737

[25] Andrade Barbosa FA, Nader G, Tokio Higuti R, Kitano C, Nelli Silva E. A simple interferometric method to measure the calibration factor and displacement amplification in piezoelectric flextensional actuators. Revista Controle & Automação. 2010; **21**(6):577-587